Article:
Zhu, H, Zhu, H, Wang, K et al. (9 more authors) (2020) Terahertz master-oscillator power-amplifier quantum Cascade laser with controllable polarization. Applied Physics Letters, 117 (2). 021103. ISSN 0003-6951

https://doi.org/10.1063/5.0013505

Terahertz master-oscillator power-amplifier quantum cascade laser with controllable polarization

Haiqing Zhu,[1,2] Huan Zhu,[1] Kai Wang, [1] Chenren Yu,[1,2] Gaolei Chang,[1,2] Fangfang Wang,[1] Jianxin Chen,[1] Lianhe Li,[3] A. Giles Davies,[3] Edmund H. Linfield,[3] Gangyi Xu,[1,4*] and Li He[1]

[1]*Key Laboratory of Infrared Imaging Materials and Detectors, Shanghai Institute of Technical Physics, Chinese Academy of Sciences, Shanghai 200083, China*

[2]*University of Chinese Academy of Sciences, Beijing 100049, China*

[3] *School of Electronic and Electrical Engineering, University of Leeds, Leeds LS2 9JT, United Kingdom*

[4] *Hangzhou Institute for Advanced Study, UCAS, Hangzhou 310024, China*

**Author e-mail address: gangyi.xu@mail.sitp.ac.cn*

Abstract

We report the realization of controllable linear-to-circular polarization states in single-mode terahertz master-oscillator power-amplifier quantum cascade lasers (THz-MOPA-QCLs). The MOPA device contains a first-order distributed feedback (DFB) laser as the master-oscillator, a preamplifier, and a 2D periodical antenna array as the power extractor. The polarization state is determined by the orientation and the phase relationship between the antennas. The antenna array is carefully designed to efficiently extract the THz radiation, and not to induce field oscillation in the array or influence the mode oscillation in the DFB section. Each demonstrated device exhibits single-mode emission with a side mode suppression ratio of ~26 dB, and a single-lobed beam with a low divergence of ~23°×30°. Realized in different devices, the degree of linear or circular polarization reaches as high as 97.5% or 99.3%. Both the operation frequency and the polarization state of the radiation are lithographically tunable.

Studies of polarized terahertz wave have attracted increasing attentions for its potential applications in spectroscopy, sensing, polarization imaging, etc.[1-5] Conventionally, the manipulation of the polarization state of terahertz radiation relies on external optical components, such as birefringent crystals,[6] wire-grid polarizers,[7] or metamaterial polarization convertors.[8-11] However, such components are usually bulky or lossy. In order to improve the miniaturization, stability and power efficiency of the optical system, it is highly desired to develop monolithic semiconductor lasers with controllable polarization. Terahertz quantum cascade lasers (THz-QCLs)[12,13] are promising semiconductor lasers, featuring high output power, high spectral purity and broadband frequency tuning.[14-22] THz-QCLs naturally emit linearly polarized radiation because of the intersubband transition of electrons in the multi-quantum wells.

Some efforts have been devoted to controlling the polarization states of the mid-infrared (MIR) or THz QCLs. Initially, orthogonal grating apertures were formed on the facet of a MIR-QCL, realizing near-circularly polarized emission at a certain position of the beam pattern.[23] In the terahertz frequency range, electrical switching of linearly polarized emission has been demonstrated in a vertical-external-cavity laser, which contains two interleaved arrays of active dipole antennas and their orientations are orthogonal to each other.[24] However, such configuration does not directly lead to an elliptical or circular polarization. Recently, by injecting two coherent beams from a phase-locked laser pair into two orthogonal antenna arrays and manipulating the intensity of each beam, monolithic THz-QCLs with dynamically tunable linear-to-circular polarization were realized.[25] Nonetheless, due to the long laser cavity involved, it is hard to precisely predict the lasing frequency and usually a few modes appear. Up to now, a THz-QCL with stable single-mode emission, controllable operation frequency and polarization state is still missing.

In this letter, we report the realization of single-mode THz-QCLs with designated operation frequency and polarization state. The devices are developed from our recently demonstrated terahertz master-oscillator power-amplifier quantum cascade lasers (THz-MOPA-QCLs),[26,27] which already exhibited stable single-mode emission with high output power and good beam quality. The MOPA device monolithically integrates a first-order distributed feedback (DFB) laser, a preamplifier, and a power extractor which usually is a grating coupler. Since the generation and extraction of THz radiation are separately controlled in different sections, and given the flexibility of the design of power extractor, the THz-MOPA-QCL is a promising platform to tailor the frequency, amplitude and wavefront of the THz

radiation. Here we exploit a 2D array of slot antennas as the power extractor, where the orientation and the phase relationship between the antennas determine the polarization state. Moreover, the antenna array is judiciously designed to guarantee efficient power extraction and, most importantly, not to induce field oscillation in the array or influence the mode oscillation in the DFB section which is crucial for high uniformity of the polarization state and high purity of the emission spectrum.

Figure 1(a) shows the scheme of the proposed MOPA device which is based on a metal-metal waveguide. The structure parameters and the SEM pictures of typical devices are given in Section 1 of the supplementary material. The GaAs/$Al_{0.15}Ga_{0.85}As$ active region is based on a bound-to-continuum design,[28] with a thickness of ~12 μm and a measured central emission frequency of ~2.7 THz. The master-oscillator (MO) section is a first-order DFB laser featuring a buried grating with a central π-shift, optimized for high seed power.[27] The intrinsic Q-factor of the fundamental longitudinal mode of the DFB grating is 492, considerably higher than those of the high-order modes. The power-amplifier (PA) section consists of three parts: a 500 μm-long straight preamplifier, a 2D array of slot antennas formed in the top metallization and an absorbing boundary. Two different types of antenna arrays are exploited, shown in Figs. 1(b) and 1(c), respectively. The first type, in which each unit cell is a single magnetic dipole antenna, is used to excite linearly polarized radiation and the polarization azimuth is determined by the orientation of the antenna. In the second type, each unit contains two magnetic dipole antennas with orthogonal orientations, and the phase relationship between them determines the DOCP (degree of circular polarization) of the resultant elliptically or circularly polarized emission. The absorbing boundary – formed by the uncovered n^+ GaAs top contact layer – efficiently absorbs the THz wave reaching the boundary.

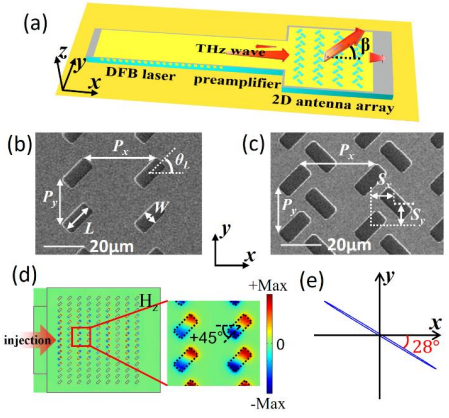

FIG. 1. (a) Schematic illustration of a THz-MOPA-QCL with controllable polarization. The gray regions correspond to the n^+ GaAs top contact layers which act as the absorbing boundaries. The red arrows show schematically the incidence, diffraction, reflection and transmission of the THz wave. Panels (b) and (c) are the SEM pictures partially showing two types of antenna arrays, which all contain 9 × 15 unit cells. The structure parameters are marked on the SEM pictures. (d) Normalized magnetic field distribution (H_z) of the first type of antenna array, in the near-field which is 2 μm above the antenna array surface. (e) Calculated polarization ellipse of the radiation at the brightest point of the beam pattern, caused by the first type of antenna array.

We now investigate the design of the first type of antenna array for a linearly polarized beam. Each antenna is a rectangular air slit (16 μm × 7 μm) and its orientation angle (θ_L) is 45° or -45° with respective to the *x*-direction, as shown in Fig. 1(b). The arrows in Fig. 1(a) schematically illustrate the diffraction, reflection and transmission of the THz wave when it is injected from the preamplifier to the antenna array. Figure 1(d) plots the calculated magnetic field (H_z) excited by the antenna array in the near-field which is 2 μm above the array surface. Because the antenna is relatively wide in order to enhance the power extraction, H_z oscillates approximately along the diagonal line of each antenna. Here, the calculations were carried out by 3D full wave finite element method (FEM) with a solver of COMSOL Multiphysics. The lateral array periodicity [P_y, as shown in Fig. 1(b)] is less than the effective wavelength in the waveguide to avoid transverse diffraction but is large enough to suppress coupling between the adjacent antennas. Since the antennas along each column (in *y*-direction) share the same phase, the subwave emitted by them features semi-cylinder-shaped wavefront which is parallel to the antenna column. The longitudinal array periodicity [P_x, as shown in Fig 1(b)] is larger than the effective wavelength and facilitates the (-1)-order of diffraction, extracting the THz radiation in an oblique direction [β, shown in Fig. 1(a)]. The design of P_x is similar to that of a 1D grating coupler since no oscillation exists in *y*-direction.[11] Here, the lasing frequency f_0 – determined by the DFB grating – is set in the middle of the third photonic band of the 2D antenna array where the group velocity of the THz wave is maximized, leading to a low reflectivity. In the frequency range near the gain peak, the calculated reflectivity is less than 4%, and the calculated radiation efficiency of the antenna array is ~36% which is mainly determined by the size and the number of the antennas. The low reflectivity is of crucial importance not to disturb the phase relationship between the antennas and not to influence the mode oscillation in the DFB section. Figure 1(e) plots the calculated polarization ellipse of the radiation at the brightest point on the beam pattern, whose DOLP (degree of linear polarization) reaches 99.9% and the polarization azimuth (θ_P) is -28°. The magnetic dipole modes

excited by the antennas have the same mode profile and are in phase along the diffraction angle β, which explain the excellent DOLP. More details of calculations are given in Section 2 of the supplementary material.

The fabrication of the THz-MOPA-QCLs is similar to that of THz-QCLs with a metal-metal waveguide,[27] where the 2D antenna array is formed in the same step of the top metallization. The devices were measured in pulsed mode (100 kHz repeated frequency, 1 μs pulse width). Figure 2(a) shows the emission spectra of 3 MOPA devices with the periodicity of the DFB grating (Λ_{DFB}) varying from 15.1 μm to 15.7 μm. The devices exhibit single-mode emission in most part of the lasing dynamic range, and the emission wavelength varies linearly with Λ_{DFB}. The results reveal that the devices operate on the DFB mode and the disturbance from the reflected wave caused by the antenna array is effectively suppressed. Figure 2(b) displays the light-current density (*L*-*J*) curves of two devices with the same Λ_{DFB} (15.4 μm) but different antenna orientations ($\theta_L = \pm 45°$), illustrating similar peak outputs of ~5.1 mW. Here, the output power was measured by a Thomas Keating terahertz power meter. Figure 2(c) presents the measured far-field beam patterns of these two devices, demonstrating that a single-lobed beam is achieved for each device and the divergent angle (full width at half maximum, FWHM) is approximately 20° × 28°. The angular definition of the far-field measurement and the comparisons between the measured beam divergence and the diffraction limit are given in Section 3 of the supplementary material.

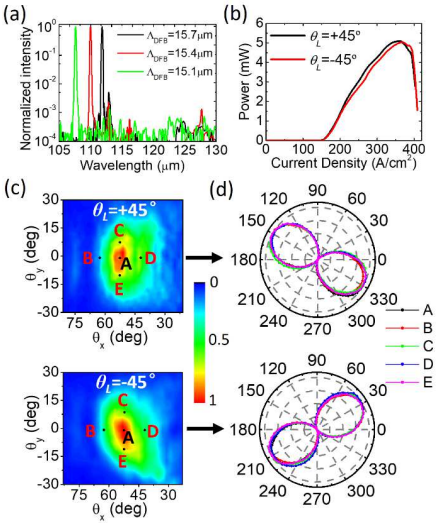

FIG. 2. (a) Emission spectra of 3 MOPA devices, where Λ_{DFB} varies from 15.1 μm to 15.7 μm and θ_L = +45°. The devices were pumped with current densities of ~263 A/cm² (Λ_{DFB} = 15.1 μm), ~346 A/cm² (Λ_{DFB} = 15.4 μm) and ~342 A/cm² (Λ_{DFB} = 15.7 μm), respectively. For two devices with the same Λ_{DFB} (15.4 μm) but different θ_L (± 45°), panels (b) and (c) show the light-current density (*L-J*) curves and the far-field emission patterns, measured at 20K. Panel (d) shows the polarization states measured at different spots on the related beam patterns marked in panel (c). The orientation angle α = 0° corresponds to +*x*-direction.

To investigate the polarization state of the radiation and its uniformity, we sequentially placed a wire-grid polarizer and a small circular aperture in front of the detector and measured the power versus the orientation angle of the polarizer at different spots on the beam pattern. The optical power was collected by a Golay cell with a solid angle of 2°. Figure 2(d) presents the measurement results at five different beam spots [marked in Fig. 2(c)] for each device, indicating linear polarizations with good uniformity. For these two devices, the values of the polarization azimuth (θ_P) are respectively 31° and -30°, and the values of the DOLP all exceed 97.5%, close to the calculation results shown in Fig. S2 in the supplementary material. Here, the DOLP is mainly limited by the noise caused by the slight vibration of the close-cycle cryostat holding the devices.

We then focus on the excitation of an elliptical or a circular polarization state. As shown in the bottom panel of Fig. 3(a), the second type of antenna array essentially contains two sub-arrays. Each sub-array is the same as the first type of antenna array, and these two sub-arrays have orthogonal orientations and are displaced by a distance (S_x along the *x*-direction and S_y along the *y*-direction). S_y is set as half of the lateral array periodicity P_y to maximize the distance between the adjacent antennas and suppress the coupling between them. Since the antennas along the y-direction share the same phase, the shift S_y will not obviously influence the polarization state. The middle panel of Fig. 3(a) presents partially the magnetic dipole mode (H_z) in the near field of the antenna array. The top panel of Fig. 3(a) shows schematically the cross section of the antenna array in the *x*-*z* plane. Along the diffraction direction ($\theta_x = \beta$, $\theta_y = 0$), each sub-array excites a linearly polarized beam, and the phase difference between these two beams is $\Delta\Phi_e = 2\pi \times S_x/P_x$. Consequently, along the diffraction direction, the electric field of the radiation excited by the whole array reads

$$\vec{E} = A_0\overrightarrow{e_1}\exp(i\omega_0 t) + A_0\overrightarrow{e_2}\exp(i\omega_0 t + i\Delta\Phi_e). \quad (1)$$

Here, the two terms at the right side of Eq. (1) correspond to the linearly polarized sub-waves excited by the two sub-arrays with the same amplitude A_0. $\overrightarrow{e_1}$ and $\overrightarrow{e_2}$ are the unit vectors pointing out the azimuths

of the two linear polarizations. Due to the non-negligible antenna width, $\vec{e_1}$ and $\vec{e_2}$ are not orthogonal to each other, and the intersection angle (θ_{pol}) is calculated to be 56°. The degree of circular polarization (DOCP) of the resultant wave can be expressed by Eq. (2), whose deduction is detailed in Section 4 of the supplementary material.

$$\mathrm{DOCP} = \left|\sin(\Delta\Phi_e)\sin(\theta_{pol})/[2\sin^2\left(\tfrac{\Delta\Phi_e}{2}\right)\sin^2\left(\tfrac{\theta_{pol}}{2}\right) + 2\cos^2(\tfrac{\Delta\Phi_e}{2})\cos^2(\tfrac{\theta_{pol}}{2})]\right|. \quad (2)$$

Experimentally, DOCP equals to $2\sqrt{I_{max}I_{min}}/(I_{max}+I_{min})$,[25,29] where I_{max} and I_{min} are the maximum and the minimum power through a polarizer when its orientation rotates.

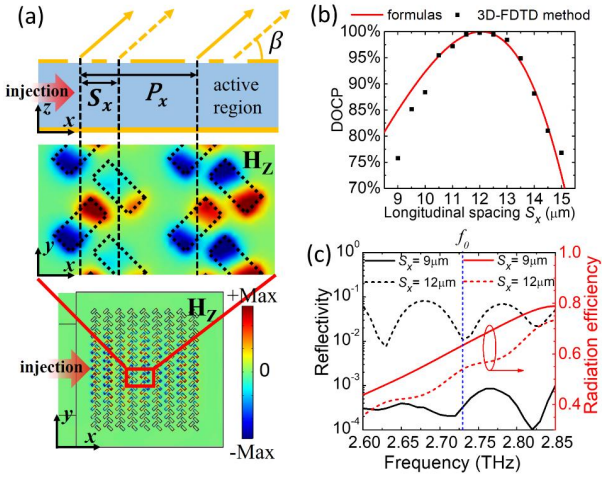

FIG. 3. (a) The top panel is the side-view of the emission condition. The middle and bottom panels are the normalized magnetic field distribution (H_z) in the near-field of the second type of 2D antenna array. (b) The DOCP as a function of S_x, in which the red curve and the black dots respectively correspond to the results calculated by Eq. (2) or by the 3D-FDTD method. (c) Reflectivity and radiation efficiency of the 2D antenna arrays, where S_x are respectively 9 μm and 12 μm. The blue dashed line corresponds to the lasing frequency f_0.

For the radiation at the brightest point on the beam pattern, Fig. 3(b) shows the variation of the DOCP versus S_x calculated by Eq. (2) or by the 3D finite-difference time-domain (FDTD) method, illustrating good agreement with each other. Experimentally, two different values of S_x (9 μm and 12 μm) were selected to generate an elliptically (DOCP = 75.8%) and a near-circularly polarized beam (DOCP = 99.9%), respectively. Figure 3(c) displays the calculated reflectivity and the radiation efficiency of these two antenna arrays, in the frequency range around the gain peak. The blue dashed line in Fig. 3(c) corresponds to the lasing frequency. It is worth noting that, when S_x is 9 μm, the reflectivity is reduced down to the

order of 10^{-3}. The main reason is that, in the frequency range considered, S_x = 9 μm is close to a quarter of effective wavelength in the waveguide. Therefore, the reflected sub-waves caused by the two sub-arrays destructively interfere with each other. Since more antennas involved in the second type array, the calculated radiation efficiencies are respectively 54% (S_x = 12 μm) and 63% (S_x = 9 μm) at the lasing frequency, larger than that of the first type array (~36%).

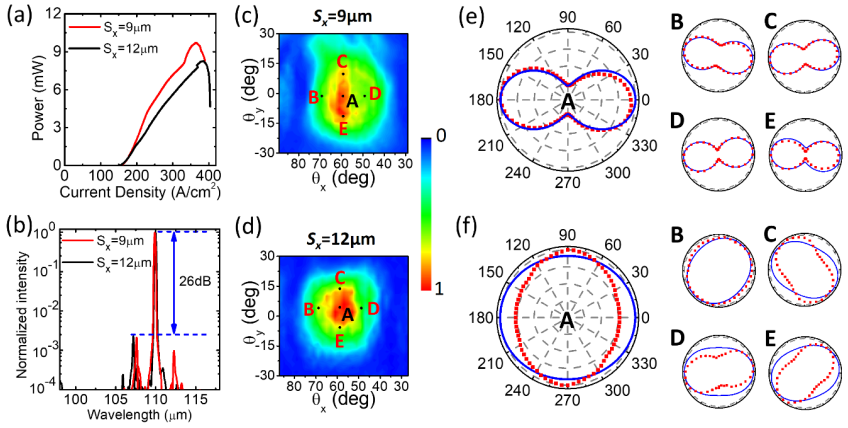

FIG. 4. (a) Light-current density (*L-J*) curves of two devices with the same Λ_{DFB} (15.4 μm) and different values of S_x (9 μm and 12 μm), measured at 20 K. (b) Emission spectra of the two devices, which were respectively biased at 339 A/cm² (S_x = 9 μm) and 299 A/cm² (S_x = 12 μm). Panels (c) and (d) are the measured far-field patterns of these two devices. Panels (e) and (f) show the collected power versus the orientation angle of the polarizer, at different spots on the beam patterns marked in the panels (c) and (d). The red dots and the blue curves respectively correspond to the measured and simulated results.

Figure 4 shows the measurement results of two MOPA devices, with the same periodicity of the DFB grating (Λ_{DFB} = 15.4 μm) but different values of S_x (9 μm and 12 μm). Fig. 4(a) shows that the peak output power of the two devices reaches 9.7 mW and 8.3 mW, respectively. As shown in Section 5 of the supplementary material, a 500 μm-long preamplifier approximately amplifies the THz power from the DFB section by a factor of 1.7. Figure 4(b) shows that the two devices exhibit single-mode emission and the side mode suppression ratio (SMSR) exceeds 26 dB. Figures 4(c) and 4(d) illustrate that these two devices show similar beam pattern with the divergence being ~25° × 33°. Figures 4(e) and 4(f) show the polarization states and their spatial uniformity of these two devices, where the red dots present the collected power through the polarizer versus its orientation angle (measured at different spots on the

related beam patterns), while the blue curves are the simulated results. At these spots, the simulated and the measured values of DOCP are given in Section 6 of the supplementary material. When S_x equals to 9 μm [Fig. 4(e)], the measured DOCP is 76.8% at the central spot [Point A in Fig. 4(c)], close to the calculated value (75.8%). For this device, at different emission directions the measured DOCP and the polarization axis agree reasonably with the simulations. When S_x is 12 μm [Fig. 4(f)], the measured DOCP reaches as high as 99.3% at the center of the beam pattern [Point A in Fig. 4(d)], suggesting a near-circularly polarized light. The polarization states vary slightly at different spots on the beam pattern, and are still in good consistence with the simulations. Note, for Spot A in Fig. 4(f), the ratio of the intensity in the *x*-axis ($\alpha = 0°$) to that in the *y*-axis ($\alpha = 90°$) was calculated to be ~1.04, and measured to be ~0.79. This marginal deviation results in the inversion of the major axis of the elliptical field distribution (*i.e.*, the collected power versus the polarizer orientation). The main reason of non-uniformity is that the phase difference $\Delta\Phi_e$ between the two linearly polarized beams – generated by the two sub-arrays – changes with the radiation direction. In fact, similar phenomena were found in the related work where an antenna array was exploited to manipulate the polarization states.[24,29,30]

It is expectable to improve the device performance in terms of the output power, the beam quality and the uniformity of the polarization state. Possible strategies include the increase of the preamplifier length, the increase of the dimensions of the antenna array and the reduction of the reflectivity caused by the antenna array. Obviously, an antenna array with large dimensions will enable a more directional beam and hence a more uniform polarization state. Moreover, reducing the reflectivity will enable using a long and tapered preamplifier to enhance the power amplification. The results in this work already indicate that the reflectivity can be dramatically reduced when S_x is close to a quarter of effective wavelength. With this optimized S_x and the related phase difference $\Delta\Phi_e$, the polarization state can still be controlled by the orientations of the antennas (i.e. θ_{pol}), as described in Eq. (2). The same strategy can be used to generate a linear polarization state by simply making the two antennas in each unit have the same orientation.

In conclusion, we realized monolithic THz-MOPA-QCLs which exhibit single-mode emission with designable operation frequency, good beam quality and controllable linear-to-circular polarization. The polarization-selective coupler developed in this work can be applied in lasers across a broad range of wavelength, and also in amplifiers and detectors for the manipulation of polarization states.

See the supplementary material for the following information: detailed structure parameters of the

THz-MOPA-QCLs, the definition and the calculations of the DOLP and DOCP, the comparison between the beam divergence and the diffraction limit, the estimation of the power amplification of the MOPA configuration, and the measurement results of the non-uniformity of the polarization.

This work was supported by National Natural Science Foundation of China (61734006, 61974151, 61574149); The Key Project of Chinese National Programs for Research and Development (2016YFB0402303, 2016YFA0202200); The Engineering and Physical Sciences Research Council (EPSRC), UK (COTS programme EP/J017671/1); The Royal Society and Wolfson Foundation.

The data that support the findings of this study are available from the corresponding author upon reasonable request.

[1] J. Xu, G. J. Ramian, J. F. Galan, P. G. Savvidis, A. M. Scopatz, R. R. Birge, J. Allen, and K. W. Plaxco, "Terahertz circular dichroism spectroscopy: A potential approach to the in situ detection of life's metabolic and genetic machinery," Astrobiology **3** (3), 489-504 (2003).

[2] M. Yamaguchi, F. Miyamaru, K. Yamamoto, M. Tani, and M. Hangyo, "Terahertz absorption spectra of L-, D-, and DL-alanine and their application to determination of enantiometric composition," Appl. Phys. Lett. **86** (5), 53903 (2005).

[3] D. Pallavi, A. Karim, S. J. Cecil, and H. G. Robert, "Detection of colon cancer by continuous-wave terahertz polarization imaging technique," J. Biomed. Opt. **18** (9), 1-4 (2013).

[4] F. Rutz, T. Hasek, M. Koch, H. Richter, and U. Ewert, "Terahertz birefringence of liquid crystal polymers," Appl. Phys. Lett. **89** (22), 221911 (2006).

[5] S. Katletz, M. Pfleger, H. Pühringer, M. Mikulics, N. Vieweg, O. Peters, B. Scherger, M. Scheller, M. Koch, and K. Wiesauer, "Polarization sensitive terahertz imaging: detection of birefringence and optical axis," Opt. Express **20** (21), 23025 (2012).

[6] R. Zhou, B. Ibarra-Escamilla, J. W. Haus, P. E. Powers, and Q. Zhan, "Fiber laser generating switchable radially and azimuthally polarized beams with 140 mW output power at 1.6 μm wavelength," Appl. Phys. Lett. **95** (19), 191111 (2009).

[7] I. Yamada, K. Takano, M. Hangyo, M. Saito, and W. Watanabe, "Terahertz wire-grid polarizers with micrometer-pitch Al gratings," Opt. Lett. **34** (3), 274 (2009).

[8] N. K. Grady, J. E. Heyes, D. R. Chowdhury, Y. Zeng, M. T. Reiten, A. K. Azad, A. J. Taylor, D. A. R. Dalvit, and H. Chen, "Terahertz Metamaterials for Linear Polarization Conversion and Anomalous Refraction," Science **340** (6138), 1304-1307 (2013).

[9] Y. Z. Cheng, W. Withayachumnankul, A. Upadhyay, D. Headland, Y. Nie, R. Z. Gong, M. Bhaskaran, S. Sriram, and D. Abbott, "Ultrabroadband reflective polarization convertor for terahertz waves," Appl. Phys. Lett. **105** (18), 181111 (2014).

[10] R. Fan, Y. Zhou, X. Ren, R. Peng, S. Jiang, D. Xu, X. Xiong, X. Huang, and M. Wang, "Freely Tunable Broadband Polarization Rotator for Terahertz Waves," Adv. Mater. **27** (7), 1201-1206 (2015).

[11] J. Lin, J. P. B. Mueller, Q. Wang, G. Yuan, N. Antoniou, X. C. Yuan, and F. Capasso, "Polarization-Controlled Tunable Directional Coupling of Surface Plasmon Polaritons," Science **340** (6130), 331-334 (2013).

[12] R. Kohler, A. Tredicucci, F. Beltram, H. E. Beere, E. H. Linfield, A. G. Davies, D. A. Ritchie, R. C. Iotti, and F. Rossi, "Terahertz semiconductor-heterostructure laser," Nature **417** (6885), 156-159 (2002).

[13] B. S. Williams, "Terahertz quantum-cascade lasers," Nat. Photonics **1** (9), 517-525 (2007).

[14] Y. Chassagneux, R. Colombelli, W. Maineult, S. Barbieri, H. E. Beere, D. A. Ritchie, S. P. Khanna, E. H. Linfield, and A. G. Davies, "Electrically pumped photonic-crystal terahertz lasers controlled by boundary conditions," Nature **457** (7226), 174-178 (2009).

[15] G. Xu, R. Colombelli, S. P. Khanna, A. Belarouci, X. Letartre, L. Li, E. H. Linfield, A. G. Davies, H. E. Beere, and D. A. Ritchie, "Efficient power extraction in surface-emitting semiconductor lasers using graded photonic heterostructures," Nat. Commun. **3** (1), 952 (2012).

[16] C. Yu, H. Zhu, F. Wang, G. Chang, H. Zhu, J. Chen, P. Chen, Z. Tang, W. Lu, C. Shen, T. Jiang, X. Wang, W. Wu, G. Xu, and L. He, "Highly efficient power extraction in terahertz quantum cascade laser via a grating coupler," Appl. Phys. Lett. **113** (12), 121114 (2018).

[17] Y. Jin, L. Gao, J. Chen, C. Wu, J. L. Reno, and S. Kumar, "High power surface emitting terahertz laser with hybrid second- and fourth-order Bragg gratings," Nat. Commun. **9** (1), 1407 (2018).

[18] S. Biasco, K. Garrasi, F. Castellano, L. Li, H. E. Beere, D. A. Ritchie, E. H. Linfield, A. G. Davies, and M.

S. Vitiello, "Continuous-wave highly-efficient low-divergence terahertz wire lasers," Nat. Commun. **9** (1), 1122 (2018).

[19] A. Khalatpour, J. L. Reno and Q. Hu, "Phase-locked photonic wire lasers by π coupling," Nat. Photonics **13** (1), 47-53 (2019).

[20] L. Bosco, M. Franckié, G. Scalari, M. Beck, A. Wacker, and J. Faist, "Thermoelectrically cooled THz quantum cascade laser operating up to 210 K," Appl. Phys. Lett. **115** (1), 10601 (2019).

[21] C. A. Curwen, J. L. Reno and B. S. Williams, "Broadband continuous single-mode tuning of a short-cavity quantum-cascade VECSEL," Nat. Photonics **13** (12), 855-859 (2019).

[22] F. Wang, V. Pistore, M. Riesch, H. Nong, P. Vigneron, R. Colombelli, O. Parillaud, J. Mangeney, J. Tignon, C. Jirauschek, and S. S. Dhillon, "Ultrafast response of harmonic modelocked THz lasers," Light: Science & Applications **9** (1), 51 (2020).

[23] N. Yu, Q. J. Wang, C. Pflügl, L. Diehl, F. Capasso, T. Edamura, S. Furuta, M. Yamanishi, and H. Kan, "Semiconductor lasers with integrated plasmonic polarizers," Appl. Phys. Lett. **94** (15), 151101 (2009).

[24] L. Xu, D. Chen, C. A. Curwen, M. Memarian, J. L. Reno, T. Itoh, and B. S. Williams, "Metasurface quantum-cascade laser with electrically switchable polarization," Optica **4** (4), 468-475 (2017).

[25] G. Liang, Y. Zeng, X. Hu, H. Yu, H. Liang, Y. Zhang, L. Li, A. G. Davies, E. H. Linfield, and Q. J. Wang, "Monolithic Semiconductor Lasers with Dynamically Tunable Linear-to-Circular Polarization," ACS Photonics **4** (3), 517-524 (2017).

[26] H. Zhu, F. Wang, Q. Yan, C. Yu, J. Chen, G. Xu, L. He, L. Li, L. Chen, A. Giles Davies, E. H. Linfield, J. Hao, P. Vigneron, and R. Colombelli, "Terahertz master-oscillator power-amplifier quantum cascade lasers," Appl. Phys. Lett. **109** (23), 231105 (2016).

[27] H. Zhu, H. Zhu, F. Wang, G. Chang, C. Yu, Q. Yan, J. Chen, L. Li, A. G. Davies, E. H. Linfield, Z. Tang, P. Chen, W. Lu, G. Xu, and L. He, "Terahertz master-oscillator power-amplifier quantum cascade laser with a grating coupler of extremely low reflectivity," Opt. Express **26** (2), 1942 (2018).

[28] S. Barbieri, J. Alton, H. E. Beere, J. Fowler, E. H. Linfield, and D. A. Ritchie, "2.9THz quantum cascade lasers operating up to 70K in continuous wave," Appl. Phys. Lett. **85** (10), 1674-1676 (2004).

[29] P. Rauter, J. Lin, P. Genevet, S. P. Khanna, M. Lachab, A. Giles Davies, E. H. Linfield, and F. Capasso, "Electrically pumped semiconductor laser with monolithic control of circular polarization," Proc. Natl. Acad. Sci. **111** (52), E5623-E5632 (2014).

[30] A. Pham, A. Zhao, Q. Jiang, J. Bellessa, C. Genet, and A. Drezet, "Interference Eraser Experiment Demonstrated with All-Plasmonic Which-Path Marker Based on Reverse Spin Hall Effect of Light," ACS Photonics **5** (3), 1108-1114 (2018).